IEEE Open Journal of the
Industrial Electronics Society

Received 9 August 2023; revised 14 September 2023; accepted 27 September 2023. Date of publication 2 October 2023;
date of current version 13 October 2023. The review of this paper was arranged by Associate Editor Antonio J. Marques Cardoso.

Digital Object Identifier 10.1109/OJIES.2023.3321239

Robust Optimization for Misalignment Tolerance in Inductive Power Transfer Coupler Design

SAMPATH JAYALATH (Member, IEEE), AND AZEEM KHAN (Senior Member, IEEE)

University of Cape Town, Cape Town 7701, South Africa

CORRESPONDING AUTHOR: SAMPATH JAYALATH (e-mail: sampath.jayalath@uct.ac.za)

This work was supported in part by the National Research Foundation of South Africa, in part by the University of Cape Town, and in part by the Department of Science and Innovation of South Africa.

ABSTRACT Coupler parameters, such as transmitter inductance (L_{Tx}), receiver inductance (L_{Rx}), and the coupling coefficient (k) or mutual inductance (M), vary with the misalignments. Their variations must be quantified and incorporated into the design and optimization stage as they impact performance indices such as efficiency and leakage magnetic field. Most of the solutions proposed in the literature compromise the performance of the coupler in search of a misalignment-tolerant design. Therefore, this article presents a method to incorporate the misalignments into the design and optimization process of an inductive power transfer (IPT) coupler by utilizing robust optimization, where misalignments are considered as noises or disturbances or uncertainties to a perfectly aligned coupler. The optimized designs resulting from this method will not compromise the performance of the coupler in search of a misalignment-tolerant design. Effectiveness of the proposed robust optimization method is experimentally verified with a 3.7 kW hardware prototype.

INDEX TERMS Coil design, coupler, electric vehicle, inductive power transfer, misalignment tolerant, optimization, robust optimization, tolerance, transformer, wireless power transfer.

I. INTRODUCTION

Inductive power transfer (IPT) technology has matured over the last few decades to find its applications in charging the batteries of mobile phones, laptops, medical implants, and electric vehicles. The recent developments in standards (STD) such as SAE J2954/1 [1], IEC 61980-1:2015 [2], and ISO 19363:2020 [3] are prime examples of recognizing this technology among the industrial partners. An IPT system consists of input-side and output-side power electronics converters to control and transfer the power through the coupler, depending on the load dynamics [4], [5]. The coupler should operate efficiently while minimizing the leakage magnetic fields to ensure living beings' safety [5], [6], [7], [8], [9]. In addition, the literature emphasizes improving the power density [9], [10] while reducing the overall cost and weight of these coils [8], [10], [13].

The EVs are expected to operate in nonideal environments where coils' misalignments are likely to occur, as shown in Fig. 1 for static wireless charging applications. The receiver coil will be misaligned longitudinally, vertically, laterally, and angularly compared to the transmitter. These misalignments impact the parameters such as transmitter inductance (L_{Tx}), receiver inductance (L_{Rx}), and the coupling coefficient (k), or mutual inductance (M), which affects the IPT system's operating performance.

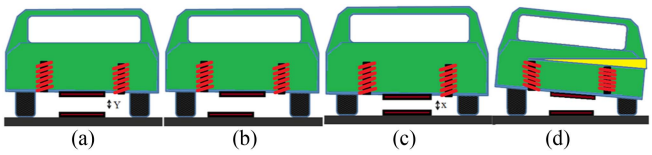

FIGURE 1. Misalignments of an EV. (a) Perfectly aligned. (b) Lateral misalignment. (c) Vertical misalignment. (d) Angular misalignment.

Several approaches are proposed in the literature to address misalignments or improve an IPT system's misalignment tolerance [14]. The first approach is through optimized circuit structures with optimal closed-loop controllers that maintain

stable output with misalignments [14], [15], [16]. Phase shift modulation of the inverter is proposed to achieve stable output with coupling and load variation [17]. DC–DC converters are used on the transmitter and receiver sides to control the input voltage of the IPT system or the equivalent output load to regulate power [18]. Alternatively, active rectifiers are proposed to control the output to achieve high efficiency [19], [20].

The second approach is to design higher order compensation topologies to realize an optimal functional relation between output variables and mutual inductances [21], [22], [23], [24], [25], [26], [27], [28]. A misalignment tolerant S-SP compensation topology with constant current or voltage characteristics is proposed in [24]. The parameters of the compensation topologies are also optimized to improve the misalignment tolerance [27]. Moreover, hybrid compensation topologies are proposed to achieve stable output current with load and coupling coefficient variations [22], [23], [28]. However, hybrid solutions are complex and inherit higher losses due to a higher number of passive components.

The third approach is to design coil structures with improved misalignment tolerance. For example, various coil structures such as circular, double DD, DDQ, bipolar, and tripolar are proposed for EV applications, and their misalignment tolerance (MT) in the three-dimensional (3-D) space varies due to different winding arrangements and geometries [5]. Couplers such as DDQ, bipolar, and tripolar have enhanced flux linkage during misalignments [5]. The fourth approach improves the misalignment tolerance of existing couplers through optimization techniques, where optimal design variables corresponding to a misalignment tolerant design are realized [13], [35], [36], [37], [38], [39]. This article's focus and contributions are toward the fourth approach.

When considering the fourth approach, the literature presents numerous multiobjective optimization strategies for couplers. Table 1 summarizes the coupler configuration, optimized objectives, and multiobjective optimization methodology of notable contributions from the literature. The proposed solutions consider multiple objectives for optimization. The common objectives considered are core loss, system cost, weight, power transfer (PT), power transfer efficiency (η), k, leakage field (B_L), efficiency between perfectly aligned and misaligned coils ($\delta\eta_M$), gravimetric power density (γ), area power density (α), and misalignment tolerances. The objectives vary in these proposed solutions due to the requirements of the optimization problem considered.

Most of these solutions do not incorporate misalignments into the optimization or design process except for the last seven designs shown in Table 1. Table 2 summarizes the type of misalignment considered, the method used to incorporate misalignment, and their advantages and disadvantages. Lateral (L), vertical (V), horizontal (H), and rotational/angular (R) misalignments of coils are considered in these studies to derive the misalignment tolerant design. There are several techniques followed to incorporate misalignments into the design flow. In [8], misalignments are considered as an objective, along with efficiency and coil costs. Mohamed et al. [13] consider the average coupling coefficient (k) during all misalignment scenarios. In [35], the lateral misalignment is regarded as a variable during the optimization in determining the optimal design variables. In [36], misalignments in six degrees of freedom are categorized into subregions, and the probability of alignment in each region is used as an index to prioritize misalignment and incorporate it into the objective function: figure of merit (FOM). In [37], the efficiency difference at misaligned and perfectly aligned operations is considered as an objective to minimize, while separate Pareto fronts are derived for perfectly and misaligned scenarios in [39]. The magnetic core size is optimized to maximize coupling with misalignments using the 3-D topology optimization technique [40].

TABLE 1. Various Optimization Solutions Proposed in the Literature

Ref	Coil Type	Objectives	Mis
[6]	Circular	Max (η) and Max (α)	No
[12]	Circular	Max (η) and Min (B_s)	No
[30]	Circular	Max (k) and Max (Q)	No
[34]	Circular	Max (η) and Min (w_{Rx})	No
[31]	Square	Max (η) Max (γ), Max (α)	No
[9]	DD	Max (η), Max (γ), Max (α) and Min (B_s)	No
[29]	DD	Max (η) and Max (α)	No
[32]	DDQ	Max (k) and Max (P_{su})	No
[8]	Circular	Max (η), Max (M_h) and Min(C_T)	Yes
[13]	DD	Max (k) and Min (System cost)	Yes
[35]	Circular	Max(MT), Min(C_L) and Min (W)	Yes
[36]	Circular	FOM (PT, η, 6DOF MT of Rx)	Yes
[37]	DD/DDQ	Max (η), Max (γ), Max (α) and Min ($\delta\eta_M$)	Yes
[39]	Rectangular	Max (η), Max (γ) and Max (α)	Yes
[40]	Circular	Max (k), Max(Φ_Z)	Yes

Note: MT: misalignment tolerance, PT: power transfer, η: efficiency, γ: gravimetric power density, α: area power density, DOF: degree of freedom, FOM: Figure of merit, M_h: Horizontal misalignment, C_T: Total cost, P_{su}: Uncompensated power, w_{Rx}: Receiver weight, C_L: Core loss, W: Weight, Φ_Z: Magnetic flux in z-direction.

The pros and cons of the proposed solutions are summarized in Table 2. One of the significant disadvantages of the proposed solutions is the performance at the aligned position is compromised in the search for a misalignment-tolerant design. Therefore, the coupler will operate below its maximum performance point as it accommodates misalignments. The root cause for it is the approach taken to define misalignment. The misalignments are considered to be an integral part of the operation. This approach will result in a compromised performance at an aligned position. However, another approach is to consider misalignments as noise or disturbance to a perfectly aligned scenario. In this approach, the performance at the aligned position is not compromised while enhancing the misalignments performances. This is the approach proposed in this article. The proposed method incorporates misalignments into the design flow without compromising the performance at the aligned position, and the best misalignment tolerant coupler is selected for prototyping.

TABLE 2. Misalignment Tolerant Optimization Strategies

Ref	Mis	Technique	Pros	Cons
[8]	H	Misalignment is considered as an objective.	Simpler method to incorporate misalignments.	Coupler performance compromised at the aligned position.
[13]	H, L, R	Average k considering all misalignments.	Improved coupling with moderate cost.	Average k compromises the coupling at the aligned position.
[35]	L	Lateral misalignment as a variable.	Minimum core loss and volume achieved.	Weak coupling compared to a uniform thickness core structure.
[36]	H, L, R	Misalignment dynamics are prioritized based on the probability of alignment in deriving the FOM objective.	Simultaneous improvement of system performance and misalignment tolerance.	Slight drop in performance at the aligned position.
[37]	V,L	The difference in efficiency between perfectly aligned and misaligned coils ($\delta\eta_M$) is considered an objective and minimized.	Identifies the superior misalignment tolerant coupler.	High computation cost with all misalignment scenarios, as algorithm search $\delta\eta_M$.
[39]	L	Pareto-fronts derived for perfectly aligned and worst-case misaligned scenarios.	Improved efficiency at both aligned and misaligned conditions.	Different designs on the Pareto fronts of perfectly aligned and worst-case misaligned scenarios.
[40]	V, L	Topology optimization of magnetic cores to ensure maximum flux linkage during misalignments.	Improved coupling coefficient compared to conventional coils.	Difficulty in fabricating the exact shape of the optimized core and the impact of other design variables of the coil are ignored.
This paper	H, R, H&R	Misalignments are incorporated into optimization by considering them as uncertainties to a perfectly aligned coupler.	It does not compromise performance in aligned and misaligned scenarios and removes designer bias in Pareto methods.	Relatively computationally expensive.

H- horizontal, L-lateral, V- vertical, R- Rotational.

The contribution of the proposed methodology compared to the literature can be summarized as follows.

1) The misalignments are considered noises or disturbances or uncertainties to a perfectly aligned coupler.
2) Introduces a method to quantify the impact of misalignment scenarios for a given objective or parameters, such as coil inductances.
3) Introduces a method to remove the designer bias in selecting a design from Pareto-front by incorporating misalignment as a means of decision-making criteria.
4) Introduces a method to incorporate misalignment into the optimization process without compromising the performances at the aligned position. The design with minimal dispersion in optimization objectives due to misalignments is identified.

In addition, the values of L_{Tx}, L_{Rx}, and k of a fabricated coupler vary from the design/optimized values due to the manufacturing tolerances of the component used for coil materials and fabrication tolerances of the coupler [6], [7]. Therefore, tolerances and uncertainties of design variables are also incorporated into the design process to present a robust optimization solution.

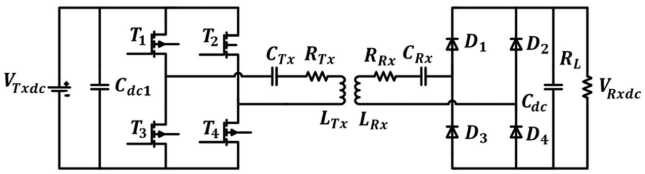

FIGURE 2. Series–series compensated IPT system.

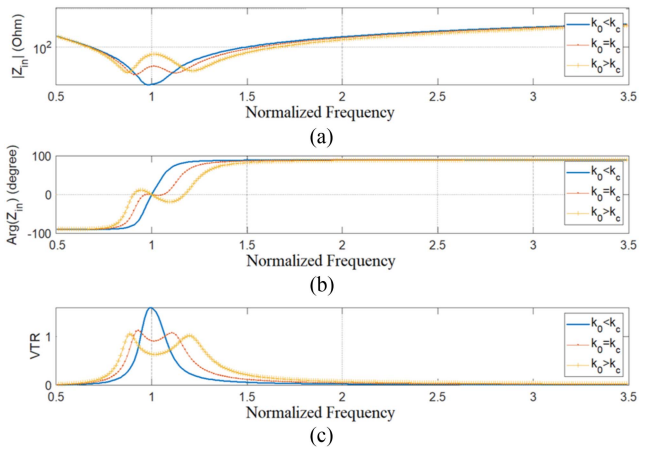

FIGURE 3. IPT system characteristics. (a) Variation of magnitude of input impedance with normalized frequency. (b) Variation of phase angle of input impedance with normalized frequency. (c) Variation of voltage transfer ratio (VTR) with normalized frequency.

II. IPT SYSTEM DESIGN AND MISALIGNMENTS

This section briefly explains the relationship between the power electronics system design and coupler parameters. Later, it introduces the various misalignments and their impact on the operations of the IPT system.

A. IPT SYSTEM DESIGN

The circuit diagram of the IPT system considered in this article is shown in Fig. 2, where series—series (SS) compensation is utilized. The subscripts Tx and Rx stand for the transmitter and receiver sides, and L, R, and C are the inductances, coil resistances, and compensation capacitances of the IPT system. The R_L is the load resistance of the system. The

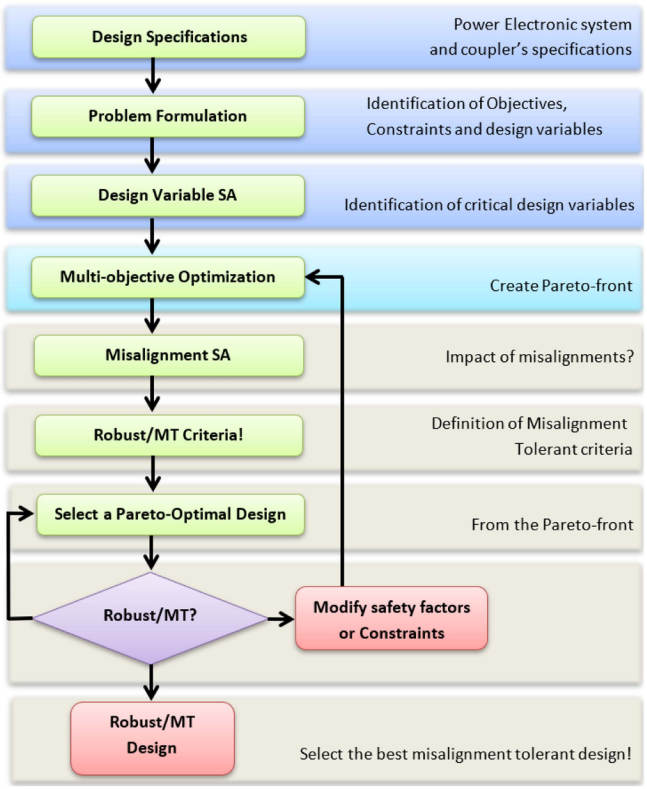

FIGURE 4. Robust optimization algorithm.

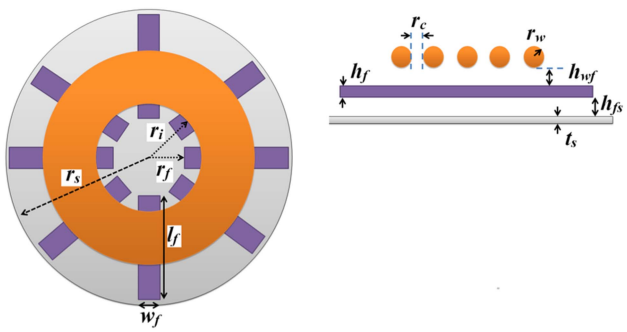

FIGURE 5. Design variables of the circular coil.

basic operating principle of an SS-compensated IPT system is derived here to understand the relationship between the power electronics system parameters and the coupler's parameters. The resonant capacitors to maximize the power transfer can be determined with $C_i = 1/(\omega_0^2 L_i)$, where i= Tx, Rx. L and ω_0 are the corresponding coil's inductance and the angular resonant frequency of the IPT system. The IPT system is modeled based on the fundamental frequency approximation since the first non-zero harmonic is 30 dBA lower than the fundamental operating frequency [6].

The load of the SS-compensated IPT system can be approximated to an equivalent resistance (R_e) given by the following:

$$R_e = \frac{8}{\pi^2}\frac{V_{Rx\mathrm{dc}}^2}{P} \tag{1}$$

where P is the power rating of the IPT system, $V_{Rx\mathrm{dc}}$ is the voltage at the terminal of the load resistance R_L or the voltage across the battery, as shown in Fig. 2. The load factor for an SS-compensated IPT system is defined as follows:

$$l_f = \frac{R_e}{\omega_0 L_{Rx}}. \tag{2}$$

The optimum load factor ($l_{,f(\mathrm{opt})}$) corresponding to maximum transmission efficiency for an SS-compensated IPT system is given by the following [6]:

$$l_{f(\mathrm{opt})} = \frac{1}{Q_{Rx}}\sqrt{1 + k^2 Q_{Tx} Q_{Rx}} \tag{3}$$

where Q_{Tx} and Q_{Rx} are the quality factors of transmitter and receiver coils. The quality factor of a coil is given by the following [5]:

$$Q_i = \frac{2\pi f E_L}{P_L} \approx \frac{2\pi f L_i}{R_i} \tag{4}$$

where i= Tx, Rx. E_L is the peak energy stored in the coil, P_L is the average power loss in winding, magnetic materials, and passive shields, and f is the operating frequency. Often, Q_i can be approximated as shown by the right-hand side of (4), assuming that core losses and shielding losses are minimal compared to winding losses. R_i is the equivalent series ac resistance of the transmitter or receiver coil with inductance L_i. The IPT systems for EVs operate at a high-frequency range of 81.38–90.00 kHz to comply with SAE J2954 [1]. Therefore, coils have a larger unloaded quality factor. For large quality factors, the $l_{f(\mathrm{opt})}$ simplifies to k. Therefore, the efficiency can be maximized if the load factor is as follows:

$$\frac{R_e}{\omega_0 L_{Rx}} \approx k. \tag{5}$$

The maximum theoretical power transmission efficiency (η_m) at the matched optimal load is given by the following [6]:

$$\eta_m \approx \frac{\mathrm{FOM}}{\left(1 + \sqrt{1 + \mathrm{FOM}}\right)^2}. \tag{6}$$

The "figure of merit (FOM)" is given by: $\mathrm{FOM} = k^2 Q_{Tx} Q_{Rx}$. Larger values of FOM result in higher transmission efficiencies. Since FOM is related to k and the quality factors Q_{Tx} and Q_{Rx}, it is beneficial to increase these parameters to achieve higher η_m. Moreover, the nominal coupling coefficient should be less than the critical coupling coefficient ($k_c = \frac{R_e}{\omega_0 L_{Rx}}$) to avoid bifurcation. Fig. 3 is used to explain the bifurcation phenomenon. The x-axis of all the subfigures in Fig. 3 is the normalized frequency derived by dividing the frequency with resonance or operating frequency. In this example, the resonance frequency is 85 kHz. Therefore, "1" on the x-axis corresponds to the resonance frequency. Fig. 3(a) shows the variation of the input impedance magnitude (Z_{in})

of an SS-compensated IPT system with frequency for coupling coefficients in distinct ranges of an SS-compensated IPT system. Fig. 3(b) and (c) show the corresponding variations in phase angle ($Arg(Z_{\text{in}})$) of input impedance and voltage transfer ratio (VTR). k_0 is the nominal coupling coefficient of a design, while k_c is the critical coupling coefficient. The bifurcation occurs if $k > k_c$, and there are two minima in Z_{in}, three zero phase angle frequencies, and two peaks in the VTR. The system will operate in the zero-current switching region instead of the zero-voltage switching region, increasing losses. However, the bifurcation is avoided by ensuring $k < k_c$. There will be a single zero phase angle, VTR, and a minimum in Z_{in}, as shown in Fig. 3. ZVS can be realized slightly above the resonant frequency as the phase angle is always positive above the resonant frequency. Furthermore, as the design's k_0 moves away from k_c where $k_0 < k_c$, the higher frequency harmonics of the transmitter current will experience a larger input impedance. Therefore, it also reduces the total harmonics distortion of the current.

Therefore, L_{Rx} is designed to satisfy the inequality given by (7) to reduce the harmonic distortion of Tx-current due to the nonlinearity of the inverter and to avoid the frequency bifurcation phenomena:

$$K_{p\min}\left(\frac{R_e}{\omega_0 k}\right) < L_{Rx} < K_{p\max}\left(\frac{R_e}{\omega_0 k}\right). \tag{7}$$

The $K_{p\min}$ and $K_{p\max}$ correspond to factor K_p's minimum and maximum values. The factor K_p is selected to be in the range of 0.65–0.85 as it has minimal impact on the maximum transmission efficiency given by (6) and is relatively constant within this range.

The transmitter coil's inductance is determined based on the desired voltage transfer ratio for a given R_e and radian operating frequency. For an optimally matched load condition, the Tx-coil inductance is given by the following:

$$L_{Tx} \approx \left(\frac{R_e}{\omega_0 k}\right)(G_v(\omega_0))^2. \tag{8}$$

The voltage gains at the fundamental angular frequency are given by: $G_v(\omega_0) = V_{Rx\text{dc}}/V_{Tx\text{dc}}$. The desired $G_v(\omega_0)$ at optimal efficiency operation should marginally satisfy the coupler's L_{Tx} and L_{Rx} as follows:

$$G_v(\omega_0) \approx \frac{R_e}{\omega_0 M} \approx \sqrt{\frac{L_{Rx}}{L_{Tx}}}. \tag{9}$$

This article considers these design rules or constraints during the finite element analysis (FEA) based optimization process.

B. MISALIGNMENT

In stationary wireless charging systems, the Tx is fixed on the floor while the Rx is on the EV. However, the position of the Rx changes depending on the dynamics of the EV and creates different misalignment scenarios. Each scenario has a different degree of freedom (DOF) in terms of the movements. These scenarios can be categorized into the following:

TABLE 3. J2954 Specifications on Misalignments [1]

Offset direction	Misalignment
Δx	± 75mm
Δy	± 100mm
Δz	(Z_{nom}-Δ_{low})->(Z_{nom}-Δ_{low})
Rotational, Roll, and Yaw	Testing at +/- 2^0,4^0 and 6^0

1) horizontal misalignment;
2) vertical misalignment;
3) angular misalignment.

Fig. 1 shows some of the misalignment scenarios of an EV. Horizontal misalignment is due to inaccurate vehicle parking in the charging zone. It occurs laterally (y-axis) and longitudinally (x-axis). The lateral misalignment is shown in Fig. 1(b). The vertical and the angular misalignment occur due to the weight distributions in a vehicle or misalignments in tires due to wear and tear, as shown in Fig. 1(c) and (d). The coupler's air gap is often fixed to abide by the ground clearance ranges defined under the J2954 std [1]. Therefore, vertical misalignment (z-axis) is any initial fixed air gap deviation. The vertical misalignment has a single DOF, as it can move only in the z-direction. The angular displacement has three DOFs (roll (θ_x), pitch (θ_y), and yaw (θ_z) along the x-, y-, and z-axes, respectively), which depend on the weight distribution of the vehicle. Therefore, misalignment (M_a) has six DOFs for an EV

$$\boldsymbol{M_a} = \left[x, y, z, \theta_x, \theta_y, \theta_z\right] \tag{10}$$

The acceptable limits of these misalignments are defined in the SAE J2954/1 STD and are listed in Table 3 [1]. The misalignments will impact the coupler's self-inductances and the coupling coefficient or mutual inductance. The impact on the power transfer can be understood by rearranging (1) using (9)

$$P = \frac{8}{\pi^2}\frac{V_{Rx\text{dc}}V_{Tx\text{dc}}}{\omega_0 M}. \tag{11}$$

The dc voltages $V_{Rx\text{dc}}$ and $V_{Tx\text{dc}}$ are adjusted accordingly to achieve the optimum efficiency operating condition under misalignment, as discussed in [41].

III. ROBUST OPTIMIZATION OF COUPLER

Fig. 4 shows the critical steps of this article's proposed robust optimization approach. The details of the steps shown in Fig. 4 are as follows:

A. DESIGN SPECIFICATION

The robust optimization is applied to a circular coupler of a 3.7 kW IPT system, which belongs to the WPT 1 power class according to the SAE J2954 [1]. However, the proposed design methodology shown in Fig. 4 can be applied to other coupler structures at different power classes. The power electronics parameters are listed in Table 4. The SS-compensated IPT system discussed in Section II is considered in this article.

TABLE 4. IPT System Parameters

Parameter	Theoretical Values	Experimental Values
Output power (P)	3700 W	3701W
Input DC link voltage (V_{Txdc})	350 V	349 V
Output DC link voltage (V_{Rxdc})	300 V	300.5 V
DC load resistance (R_L)	24.32 Ω	24.3 Ω
Equivalent AC resistance (R_e)	19.72 Ω	19.69 Ω
Operating frequency (f)	85 kHz	85 kHz

ANSYS Maxwell software is used to model the IPT coupler and determine parameters such as k, L_{Tx}, and L_{Rx} and the objectives' values (efficiency and leakage field). The coils are analyzed using a 3-D FEA model.

B. PROBLEM FORMULATION

Once the design specifications are identified, the multiobjective optimization problem is formulated. The problem formulation consists of the following steps.

1) DESIGN OBJECTIVES IDENTIFICATION

Objectives such as power transmission efficiency (η_m) given by (6) and leakage magnetic fields (B_L) depend on parameters such as k or M, L_{Tx}, and L_{Rx}. However, misalignments alter these parameters and hence will impact the objectives. Therefore, this paper considers maximizing η_m and minimizing B_L as the objectives for optimization.

$$f_{\eta_m}\left(d_1, d_2, \ldots..d_{k_d}\right) \rightarrow \max \tag{12}$$

$$f_{B_L}\left(d_1, d_2, \ldots..d_{k_d}\right) \rightarrow \min \tag{13}$$

where $d_1, d_2, \ldots..d_{k_d}$ are design variables of the coils as elaborated in Section III-B3. The ANSYS Maxwell 3-D is used to simulate the couplers and derive the transmission efficiency of coils. The coupler losses consist of winding losses, losses in the magnetic material, and passive shielding losses. MnZn Ferrite (HP400 from Mahindra) and aluminum are the magnetic and passive shield materials used in this optimization. Litz wire with 800 strands of AWG 37 is used for the coil winding. Loss characteristics of MnZn ferrite material used are incorporated into ANSYS Maxwell to determine core losses. The ac resistance considers the skin effect and the internal proximity effect. Winding losses are determined using this ac resistance and current through the coils at the resonant frequency. At the same time, eddy current losses are also determined using the ANSYS Maxwell software's eddy current solver.

2) DESIGN CONSTRAINTS IDENTIFICATION

The coupler design constraints are extracted from the SAE J2954 STD, industrial practices, and power electronics system design. The constraints resulting from the design of the SS-compensated IPT system are considered during the optimization to restrict parameters such as k, L_{Rx}, and L_{Tx} in the FEA domain. The L_{Rx} must satisfy the inequality given by (7)

$$K_{p\min}\left(\frac{R_e}{\omega_0 k}\right) < L_{Rx}\left(d_1, d_2, \ldots, d_{k_d}\right) < K_{p\max}\left(\frac{R_e}{\omega_0 k}\right). \tag{14}$$

While the L_{Tx} must satisfy the inequality given (8)

$$L_{Tx}\left(d_1, d_2, \ldots, d_{k_d}\right) = \left(\frac{R_e}{\omega_0 k}\right)\left(G_v\left(\omega_0\right)\right)^2. \tag{15}$$

The coupling coefficient is limited to less than the critical coupling coefficient to avoid bifurcation

$$k\left(d_1, d_2, \ldots, d_{k_d}\right) < k_c. \tag{16}$$

The air gap is limited to 150 mm

$$l_g\left(d_1, d_2, \ldots, d_{k_d}\right) = 150 \text{ mm}. \tag{17}$$

A nominal operating frequency of 85 kHz is used within the 81.38–90.00 kHz [1]

$$f\left(d_1, d_2, \ldots, d_{k_d}\right) = 85 \text{ kHz}. \tag{18}$$

The maximum coil area is restricted to 0.30 m^2 by considering the coil dimensions required to transfer power over an air gap of 150 mm [1]

$$A_c\left(d_1, d_2, \ldots..d_{k_d}\right) < 0.30 \text{ m}^2. \tag{19}$$

The flux density of the ferrite bars is restricted to a maximum of 200 mT to avoid saturation

$$\text{FE}_{\text{sat}}\left(d_1, d_2, \ldots..d_{k_d}\right) < 200 \text{ mT}. \tag{20}$$

Table 5 summarizes these constraints.

TABLE 5. IPT System Constraints

Parameter	Value
Coil area (A_c)	<0.30 m^2
Air gap (l_g)	150 mm
Operating frequency (f)	85 kHz
Flux density of Ferrite bars(FE_{sat})	<200 mT
L_{Rx}	Equation (14)
L_{Tx}	Equation (15)

3) DESIGN VARIABLES DEFINITION

The circular coil design variables are shown in Fig. 5. The design variables vector is given by the following:

$$\begin{aligned} d &= \left[d_1, ., d_{k_d}\right] \\ &= \left[r_w, r_i,\ r_c,\ l_f,\ h_f\ , w_f,\ h_{wf},\ h_{fs},\ t_s,\ r_s,\ r_f,\ N\right] \end{aligned} \tag{21}$$

where r_w and r_s are the radius of the conductor and the shield, r_i and r_f are the starting radius of the coil and the ferrite bars, r_c, h_{wf}, and h_{fs} are the separations between the two adjacent conductors, the conductor, and the ferrite bar and the shield and the ferrite bar. l_f, w_f, and h_f are the ferrite bars' length, width, and thickness. t_s is the thickness of the shield, while N is the number of turns.

The design variables' ranges are listed in Table 6. The design variables with subscript T in Table 6 correspond to the

TABLE 6. Design Variables of the Coupler

Variable	LB(mm)	UB (mm)	COV	Design 1	Design 3
r_{iT}/r_i	75	150	1	110/102	113/100
r_{wT}/r_w	1	2.5	1	1.95/2.05	1.98/2.10
r_{cT}/r_c	0.5	8	25	0.2/0.8	0.6/1.5
r_{sT}/r_s	267	320	1	300.5/298	297/300.2
h_{wfT}/h_{wf}	0.5	5	7.75	3.74/3.74	3.74/3.74
h_{fsT}/h_{fs}	0.5	5	10	2.5/2.5	2.5/2.5
t_{sT}/t_s	0.4	2	17.5	2.04/2.2	2/2.02
r_{fT}/r_f	80	98	4	81/81.2	80.4/81
N_T/N_R	12	20	NA	18/14	18/14
t_{fT}/t_f	25		0.78	25/25	25/25
w_{fT}/w_f	25		0.78	25/25	25/25
l_{fT}/l_f	202		0.25	202/202	202/202

transmitter coil values, while the others correspond to receiver coil values.

4) DESIGN VARIABLE'S TOLERANCES

These design variables are associated with manufacturing and fabrication tolerances. Manufacturing tolerances are variations in ferrite, litz wire, and shielding material dimensions due to imperfections in the manufacturing process. Fabrication tolerances are mainly due to difficulties in accurately realizing design variables such as space between the turns. The coefficient of variation (COV) of design variables is defined to incorporate the tolerances of design variables into the design process. COV is the ratio between the design variables' standard deviation (SD) and mean value with a normal distribution. COV of this study is provided in Table 6. The process capability index is used to determine the SD of the manufacturing process

$$C_{pK} = \min\left[\frac{U_{SL}-\mu}{3\sigma}, \frac{\mu - L_{SL}}{3\sigma}\right]. \tag{22}$$

The upper and lower tolerance limits are U_{SL} and L_{SL}. C_{Pk} for an established manufacturing process is around 1.33.

Once the problem is formulated, as discussed above, the next optimization step is the sensitivity analysis (SA), as shown in Fig. 4.

C. DESIGN VARIABLE SENSITIVITY ANALYSIS

The SA identifies important design variables related to the optimization objectives and constraints. The design of the experiment approach is used to evaluate the reliability of the numerical model. The Latin hypercube sampling (LHS) is used to scan the multidimensional input variables to create the meta-model of optimal prognosis (MOP) [42]. This model can represent the original problem, and model accuracy can be verified by evaluating the coefficient of prognosis [43]. A Latin hypercube is an m-dimensional object representing m different analyzed design variables.

Design variables are listed in Table 6, and 100 FEA designs were solved to create the MOP. Furthermore, the MOP can be used to analyze various design configurations without additional simulations. This feature of the MOP is useful for optimization problems solved through FEA due to their high computational cost. Table 7 lists each variable's contribution percentage towards the objectives (η_m and B_s) and constraints (L_{Tx}, $L_{Rx,}$ and k) derived from the MOP. It is the relative indication of a variable's impact on objectives and constraints. For example, the receiver side r_i has a 15.5% impact on efficiency, while r_c has 13.5% on efficiency.

TABLE 7. Coefficient of Prognosis Matrix for Design Variables

Parameter	*Objectives*		*Constraints*		
	η_m	B_s	L_{Tx}	L_{Rx}	k
r_i	15.5	30.6	*NA*	84.9	14.3
r_w	4.1	0.8	*NA*	3.1	8.5
r_c	13.5	18.7	*NA*	10.4	43
r_s	1.4	0.6	*NA*	0	0
r_f	1.2	0.2	*NA*	0	0
h_{wf}	0	0.4	*NA*	1.3	0
h_{fs}	0	0	*NA*	0	0
t_s	1.3	0.3	*NA*	*0*	0
r_{iT}	20.2	27.8	51.2	*NA*	8.6
r_{wT}	4.2	0.5	9.2	*NA*	1.1
r_{cT}	32.5	17.7	37.1	*NA*	23
r_{sT}	3.1	0.4	0	*NA*	0
r_{fT}	1.2	0.4	0	*NA*	0
h_{wfT}	0	0	1.3	*NA*	0
h_{fsT}	0	0	0	*NA*	0
t_{sT}	1.5	0.4	0	*NA*	0

Therefore, when looking into the percentage contributions, the design variables r_i, r_w, and r_c of the *Tx*-coil and the *Rx*-coil have the highest impact on the efficiency, leakage magnetic field, coil inductances, and coupling coefficient. The design variables such as h_{wf}, h_{wfT}, h_{fs}, h_{fsT}, t_s, and t_{sT} have the least contribution toward the objectives and constraints, as shown in Table 7, with low percentage contributions. Therefore, these design variables are kept at their nominal values, as they contribute little improvements (as identified by percentage contribution in Table 7) at the expense of higher computational cost. However, in this article, h_{wf}, h_{wfT}, h_{fs}, and h_{fsT} are the only design variables kept constant at their initial nominal values, as the computational cost was not a major limitation due to high-performance computing availability.

The variations of objectives, constraints, and parameters due to design variables can also be derived from sensitivity analysis, as shown in Fig. 6. Fig. 6(a) shows the variation of efficiency with design variables r_c and r_i of the Rx coil. Fig. 6(b) shows the efficiency variation for the Tx coil. Fig. 6(c) shows the coupling coefficient variation with the Tx coil's r_c and r_i. The results are interpolated to visualize the pattern depicted by each response. The next step of the design flows is multiobjective optimization, as shown in Fig. 4.

D. MULTIOBJECTIVE OPTIMIZATION

The multiobjective optimization (MOO) is performed for objectives (12) and (13) for design variables defined in (21).

The Pareto-front of size m derived using each n iteration of the optimization algorithm is given by the following:

$$P_n = \left\{f_{1ju}, \ldots\ldots, f_{aju}\right\} | u \in \mathbb{N}, 1 \le u \le m. \tag{23}$$

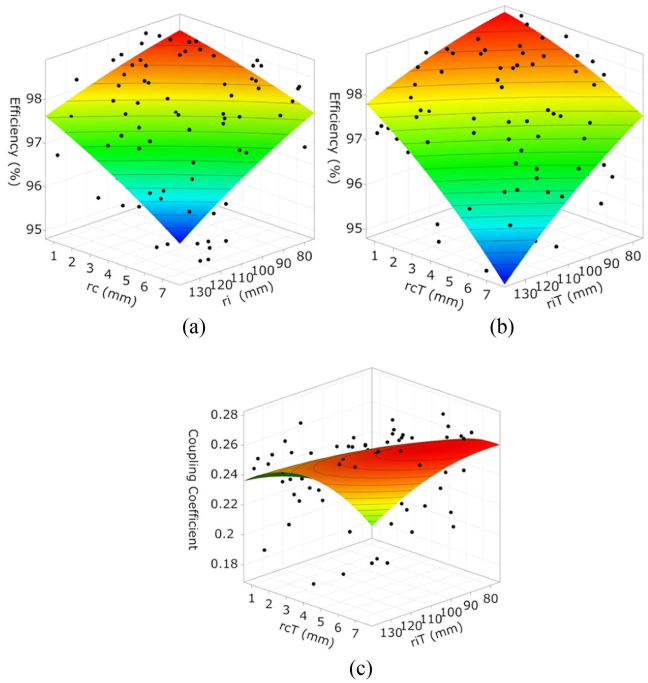

FIGURE 6. Impact of design variables on the responses. (a) Efficiency with r_c and r_i. (b) Efficiency with r_{cT} and r_{iT}. (c) Coupling coefficient with r_{cT} and r_{iT}.

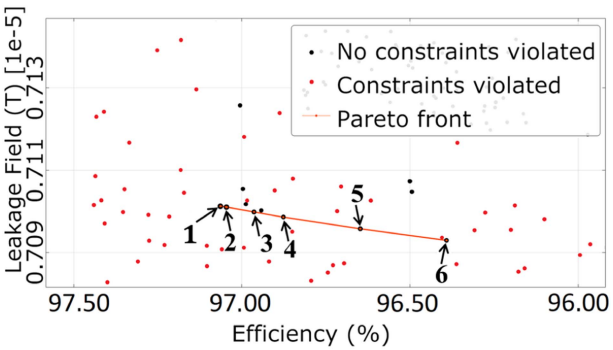

FIGURE 7. Pareto-front of the multiobjective optimization.

This study uses the non-dominated sorting genetic algorithm II (NSGA-II) to derive the Pareto-front. NSGA II is preferred as it has fast and efficient convergence and can search a wide range even if the starting solution is unfeasible. Fig. 7 shows the multiobjective optimization's Pareto-front (red line) with Pareto optimal designs labeled as 1, 2, 3, 4, 5, and 6. Black dots not on the Pareto front represent non-Pareto optimal designs that did not violate any constraints. Red dots represent the designs that violate the constraints identified in Section III-B2. These designs are ignored when deriving the Pareto-front.

E. MISALIGNMENTS

This section explains how misalignments are incorporated into the design flow.

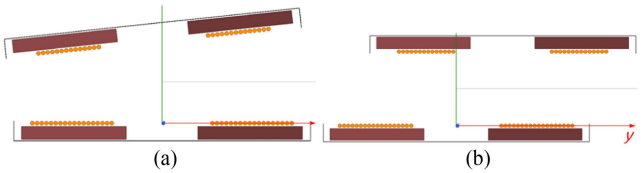

FIGURE 8. Misalignment scenarios of a circular coupler. (a) Angular misalignment. (b) Horizontal misalignment.

TABLE 8. Coefficient of Prognosis Matrix for Misalignment

	k	L_{Tx}	L_{Rx}
Δx=Δy	94.4	98.2	97.5
θ	5.3	1.5	1.9

1) DEFINITION OF MISALIGNMENTS

Initially, misalignments considered in the optimization problem are identified. This article assumes the circular coupler's angular misalignment has a single DOF, where $\theta_x = \theta_y = \theta$. The horizontal misalignment in the y-direction is considered as it has the maximum offset limit compared to the x-direction according to the SAE J2954 standard [1]. Fig. 8 shows the 2-D side views of the circular receiver coil's angular and horizontal misalignments considered in this article. In addition, the combinations of angular and horizontal misalignments are also considered.

2) MISALIGNMENT SENSITIVITY

Misalignment sensitivity analysis is performed on an optimized design on the Pareto-front shown in Fig. 7 to identify the impact of misalignments on k, L_{Tx}, and L_{Rx}. The method followed here is similar to the design variables sensitivity analysis explained in Sections III-C. The results are listed in Table 8 in terms of the percentage contribution of each misalignment on parameters k, L_{Tx}, and L_R. The horizontal misalignment significantly impacts the k, L_{Tx}, and L_{Rx} compared to angular misalignment, as seen in Table 8.

The variations of k, L_{Tx}, and L_{Rx} due to misalignments can also be derived from misalignment sensitivity analysis, as shown in Fig. 9. Fig. 9(a) shows the coupling coefficient's variation with angular and horizontal misalignment, and it reduces significantly with the horizontal misalignments (Delta x). The impact of angular misalignment is minimal. Fig. 9(b) and (c) show the variation of the L_{Tx} and L_{Rx} with misalignments, where both show similar behavior, and the impact of horizontal misalignment is dominant compared to angular misalignment. The variations shown in Fig. 9 complement the results listed in Table 8. Therefore, the misalignment sensitivity analysis provides an overall idea of the coupler's responses with respect to misalignments and will be used to define the misalignment tolerance evaluation criteria in the next section.

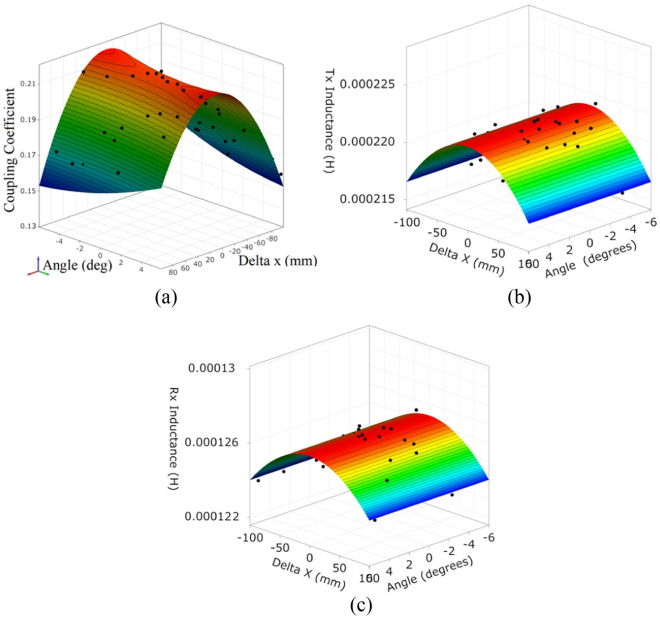

FIGURE 9. Impact of misalignments on (a) coupling coefficient, (b) transmitter inductance, (c) receiver inductance.

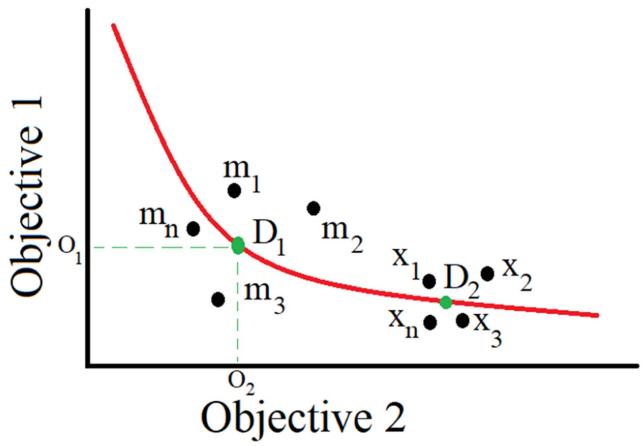

FIGURE 10. Impact of misalignment on Pareto-front.

3) MISALIGNMENT TOLERANT CRITERIA

Fig. 10 shows an example of a Pareto-front for two objectives. Design 1 and design 2 correspond to two Pareto-optimal designs on Pareto-front derived from MOO. These designs are similar to designs 1–6 shown in Fig. 7. Design 1's optimal objective 1 and objective 2 values are O_1 and O_2. The optimal design 1 on the Pareto-front will deviate from their optimal operating point (O_1, O_2) due to misalignments to a new operating point as indicated by m_1,m_2,m_3 …., m_n on Fig. 10. m_n is the nth Pareto-optimal design. A similar deviation will occur for Pareto-optimal design 2 as shown by their new operating points x_1,x_2,x_3 ….,x_n. However, this dispersion due to misalignment will vary from one optimal design to another, as shown in Fig. 10 for design 1 and design 2. Design 1 has a high dispersion compared to design 2.

In this article, power transmission efficiency and leakage field are functions of the parameters k, L_{Tx}, and L_{Rx}, as seen in (6). Therefore, minimizing dispersion on these parameters will reduce dispersion in power transmission efficiency and leakage field objectives. Thus, the SD in the k, L_{Tx}, and L_{Rx} is considered as the indices to measure a design's robustness against misalignments or misalignment tolerance. The variation in L_{Tx} and L_{Rx} due to misalignments is minimal compared to k, as shown in Fig. 9, and misalignment sensitivity analysis results in Table 8. Therefore, the SD of k is prioritized compared to L_{Tx} and L_{Rx}. The SD for each parameter can be derived using the following:

$$\sigma_P = \sqrt{\frac{\sum (y_i - \mu)^2}{N}} \tag{24}$$

where σ_P is the SD of the parameter. y_i is each value of the dataset, while μ and N are the mean and size of the dataset. The limits of the L_{Rx} given by design (14) can also be violated due to both design variables' tolerances and misalignments. These influences can be defined as follows:

$$X = \left[X_1, X_1, \ldots., X_{k_r}\right]^T. \tag{25}$$

The probability of violating the limits defined by (14) due to misalignments and design variable tolerances is calculated to ensure the selected design's conformity with the requirements of the power electronics design. This can be expressed as follows:

$$1 - \frac{P(\mathcal{F})}{P^T(\mathcal{F})} \geq 0. \tag{26}$$

$P^T(\mathcal{F})$ is the target probability and $P(\mathcal{F})$ is the probability of failure. Therefore, the design with minimum SD in coil parameters in the order of k, L_{Rx}, and L_{Tx} within the limits of L_{Rx} given by (14) is considered the best misalignment tolerant design for implementation.

4) MISALIGNMENT METHODOLOGY

The proposed method to incorporate misalignments is implemented as follows: The misalignment tolerance of each optimized designs 1 to 6 on the Pareto-front shown in Fig. 7 is evaluated with 100 FEA designs sampled with advanced LHS [44], [45], [46], [47]. In this method, each optimized design on the Pareto-front will be subjected to 100 different misalignment combinations. The LHS distribution can accurately predict the outputs of the possible designs based on a relatively small sample of the FEA simulations. Table 9 lists the SD of each optimized design on the Pareto-front due to misalignment scenarios. Design 3 exhibits the minimum SD in k and L_{Rx} with misalignments and tolerances of design variables.

Furthermore, the probability distribution of the L_{Rx} of design 3 with misalignments is shown in Fig. 11. The conformity of the design with respect to the upper and lower limit of L_{Rx}

TABLE 9. Mean and Standard Deviation of Optimized Designs

	L_{Tx}		L_{Rx}		k	
D#	μ	σ (10^{-6})	μ	σ (10^{-6})	μ	σ
1	223.33	5.558	134.43	4.072	0.225	0.0166
2	217.53	5.554	134.21	4.052	0.233	0.0156
3	228.4	5.556	127.77	3.972	0.220	0.0124
4	221.36	5.550	126.3	3.998	0.227	0.0150
5	227.37	5.560	120.12	3.982	0.221	0.0138
6	230.50	5.568	116.21	3.962	0.218	0.0146

Note: μ: mean, σ: Standard deviation.

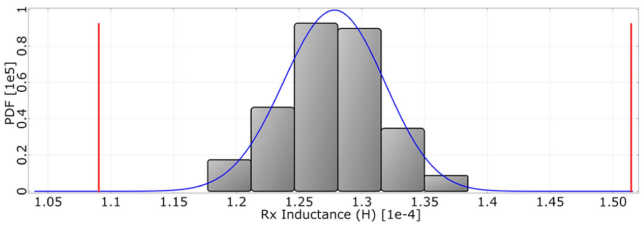

FIGURE 11. Probability density function of receiver-side inductance (L_{Rx}).

given by (14) is calculated in terms of sigma levels. Sigma level measures how a design varies from the perfect/optimized design, based on the number of defects or violations per million designs. The short-term reliability is evaluated in this article, where a target of 4.5 sigma (4.5 σ) is considered for the upper and lower limit of L_{Rx} given by (14) [44], [45]. 4.5 sigma corresponds to a probability of $P(\mathcal{F}) = 3.40 \times 10^{-6}$ or 3.4 violations per million in the short term due to the variation of the design variables' misalignments and tolerances. This is also the target probability defined in (26). The calculated upper bound is 5.02 σ, while the lower bound is 4.62 σ for design 3, as shown in Fig. 11. The upper bound and lower bound are shown in red color. Therefore, it is safe to assume that the robust criterion of 4.5 σ is achieved by design 3 with misalignments.

Designs 1, 2, 4, 5, and 6 are Pareto optimal. However, these designs have a higher SD in k and L_{Rx} than design 3 as shown in Table 9. The minimum SD in k, L_{Rx}, and L_{Tx} are prioritized criteria in selecting the best misalignment tolerant design, as discussed in Section III-E-3. Therefore, designs 1, 2, 4, 5, and 6 will not be the best misalignment tolerant design. Design 1 has the highest SD in k. Therefore, design 1 is compared with the misalignment tolerant design 3 to demonstrate the efficacy of the proposed method in Section IV. 945 FEA simulations were required to derive the misalignment tolerant design using the proposed methodology.

In a scenario where all the designs do not conform to the robust or misalignment tolerance criteria, the safety factors or constraints must be modified, as shown in Fig. 4. Multiobjective optimization is performed again to obtain the new Pareto front. As discussed above, the same design steps are followed to select the misalignment tolerant design. A misalignment-tolerant design can often be realized with a second iteration. However, this optimization problem did not require a second iteration.

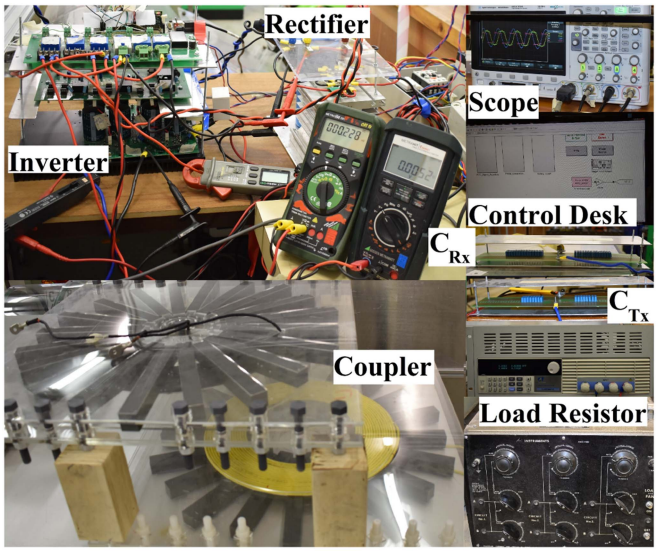

(a)

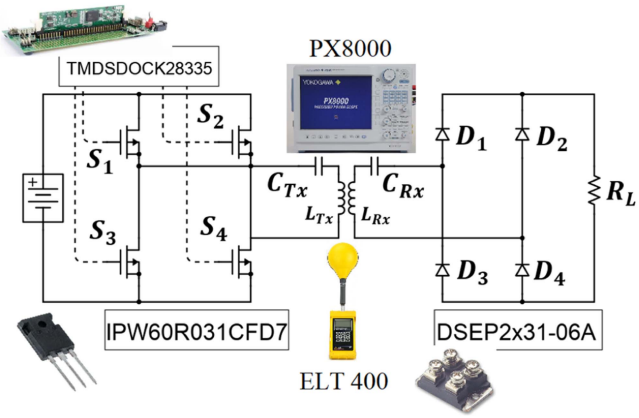

(b)

FIGURE 12. 3.7 kW hardware prototype. (a) Subsystems of the prototype. (b) Measurement devices, semiconductors, and the controller.

IV. EXPERIMENTAL VERIFICATION

Designs 1 and 3 are selected for implementation to validate the efficacy of the proposed methodology in a 3.7 kW hardware prototype. The design variables of the coils are listed in Table 6. The coils are manufactured using a litz wire with 800 strands of AWG 37. MnZn Ferrite (HP400 from Mahindra) with a permeability of 2200 is used as the magnetic material for the core. Aluminum (Al) is used for the passive shield. Moreover, the air gap of both designs is 150 mm, with an area of less than 0.3 m^2.

A. EXPERIMENTAL SETUP DETAILS

Fig. 12(a) shows the experimental setup, which includes the input-side inverter, output-side rectifier, load resistor, resonant capacitors (C_{Tx} and C_{Rx}), and the coupler. Fig. 12(b) shows the measurement instruments, semiconductor devices, and controller board used in the experimental setup. The power electronics system parameters corresponding to the

TABLE 10. Optimization and Experimental Results

Res	Design #1			MT design #3		
	Sim	Exp	Δ	Sim	Exp	Δ
L_{Tx} (μH)	223.33	229.58	+6.25	228.40	236.98	+8.58
R_{Tx} (Ω)	0.152	0.155	+0.003	0.154	0.158	+0.004
Q_{Tx}	785	791	+6	792	801	+9
C_{Tx} (nF)	15.69	15.25	–0.44	15.35	14.75	+0.60
L_{Rx} (μH)	134.43	135.10	+0.67	127.69	130.82	+3.13
R_{Rx} (Ω)	0.091	0.096	0.005	0.088	0.091	0.003
Q_{Rx}	789	751	–38	775	768	–7
C_{Rx} (nF)	26.08	26	–0.08	27.46	26.75	+0.71
M_0 (μH)	38.98	40.33	+1.35	37.57	40.074	+2.504
k_c	0.274	0.273	–0.001	0.289	0.282	–0.007
k_0	0.225	0.229	+0.004	0.220	0.227	+0.007
$k_{0(min)}$	0.148	0.150	+0.002	0.158	0.160	+0.002
Δk	0.077	0.079	+0.002	0.062	0.067	+0.005
η(%)	97.05	96.95	–0.1	96.96	96.90	-0.06
B_L (%)	7.102	7.70	+0.598	7.10	7.78	+0.68

Note: *Res: responses, Sim: Simulations, Exp: Experimental results, Δ: difference.

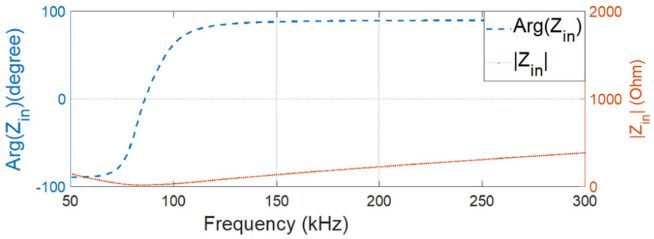

FIGURE 13. Magnitude of input impedance($|Z_{in}|$) and zero phase angle of input impedance ($Arg(Z_{in})$) of the optimized design 3.

experimental setup with design 3 are provided in Table 4. Similar values were used for the experimental setup with design 1. 1 nF of EPCOS metalized polypropylene film capacitors are used to realize the resonant capacitances (C_{Tx} and C_{Rx}) values of each design given in Table 10. The input dc-link voltage at rated power 3.7 kW is 349 V. A three-phase source is rectified to obtain the dc voltage. CoolMOS^{TM} IPW60R031CFD7 power MOSFETS are used for the inverter. Two MKPC.4B 1.5 μF snubber capacitors are used to protect the inverter switches from switching stresses. The operating frequency of the IPT system is 85 kHz and complies with the operating frequency range defined in SAE J2954 STD [1]. Two modules of IXYS DSEP2x31-06A, fast recovery diodes, are used in the rectifier. The output DC voltage across the rated load ($R_L = 24.3\ \Omega$) is 300.5 V. ELP/DCM9715 electronic load, and a custom-manufactured variable load with a rated power of 7.2 kW are used to model the load or output resistor (R_L). TMS320F28335 DSP controller is utilized to implement the control and generate switching signals for the inverter.

Yokogawa PX8000 precision power scope with Agilent N2782B AC/DC probes and Tektronix differential p5200 voltage probes were used to measure the efficiency. IPT systems are usually low power factor systems, and PX8000 supports measurements of such systems at high frequencies. The deskew function of the PX8000 was used to compensate for the differences between current waveform and voltage waveform due to measurement sensors and input characteristics of a small power factor IPT system. Agilent Technologies 3000 DSO-X 3014A captured the voltage and current waveforms of the IPT system. The couplers' leakage field is measured using a Narda ELT 400 magnetic field meter.

B. ALIGNED PERFORMANCE EVALUATION

The simulated and experimental results are listed in Table 10. The coupling coefficients of designs 1 and 3 are 0.227 and 0.229, at nominally aligned positions. These values are less than the critical coupling coefficients shown in Table 10. Therefore, frequency bifurcation is avoided. This is achieved by incorporating the inequality (16) into the optimization process. The phase angle and magnitude of the input impedance of the IPT system with the fabricated design 3 are shown in Fig. 13. The system has a single zero phase angle, as it avoids the bifurcation phenomenon.

Table 10 also lists the parameters and objectives of the fabricated coils corresponding to designs 1 and 3. The L_{Tx}, L_{Rx}, ac resistance of the transmitter (R_{Tx}), ac resistance of the receiver (R_{Rx}), M_0, and k_0 coil parameters are measured at aligned positions using an LCR meter. The coil parameters vary slightly compared to the optimized/simulated parameters due to manufacturing and fabrication tolerances of the design variables, as shown by parameter difference (Δ) in Table 10. Moreover, the ac resistances of receiver and transmitter coils are lower due to the use of litz wire. The quality factors of the transmitter and receiver are also provided in Table 10. Both coils have a high-quality factor at 85 kHz. High-quality factors are required to achieve higher efficiency, according to (6). The slight variations in simulated and experimental quality factors are due to inaccuracies in estimating the ac resistance of the coil and variations in inductances from the simulated values during coil fabrication.

The objectives η and B_L correspond to the efficiency and the leakage magnetic field measured at 650 mm from the center of the coupler at the aligned position. The transmission efficiency at the aligned position of design 3 is ∼96.90%, and design 1 is ∼96.95%. These values are almost equal to the optimized values on the Pareto-front, as shown in Fig. 7.

The measured leakage field of coupler design 3 is 7.78 and 7.40 μT for design 1. These values are about 0.68 μT (design 3) and 0.598 μT(design 1) higher than the Pareto-optimal designs, as shown in Fig. 7. The leakage fields of both designs are well below the upper limit of 27 μT defined in the SAE J2954 STD or ICNIRP guidelines [1], [2]. The input and output side current and voltage waveforms ($i_{Tx}(t)$, $i_{Rx}(t)$, $v_{Tx}(t)$, and $v_{Rx}(t)$) of the IPT system with coupler design 3 or misalignment tolerant design are shown in Fig. 14. Efficiency and leakage field results verify that the design operates as intended in the aligned position.

Additionally, the transmission efficiency of both designs at aligned positions is evaluated by varying the load resistance (R_L) from 2 to 25 Ω. Fig. 15 shows the variation of transmission efficiency with load resistance. Designs 1 and 3 reach

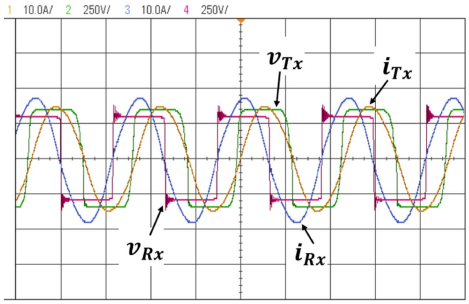

FIGURE 14. Current and voltage waveforms of the IPT system.

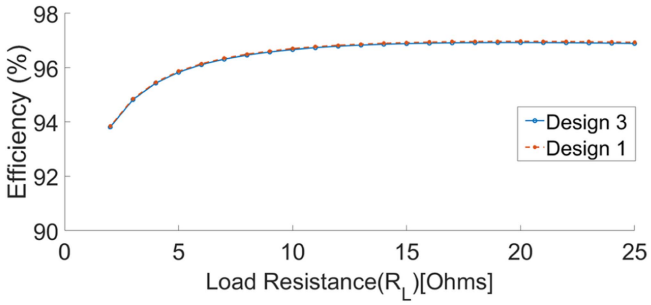

FIGURE 15. Variation of transmission efficiency with load resistance.

maximum efficiency at 20 Ω. This maximum efficiency is 96.92% for design 3 at 20 Ω, while 96.96% for design 1. The efficiencies at rated load ($R_L = 24.3$ Ω) are 96.95% and 96.90% for designs 1 and 3. The efficiency variation between 20 Ω and the rated load is less than 0.05% for both designs. High-frequency profiles over wide load variation attest to the quality of the optimization solutions derived in this work.

C. MISALIGNMENT PERFORMANCE EVALUATION

The horizontal, angular, and combinations of angular and horizontal misalignments are evaluated using the hardware prototype. Twenty-one misalignment measurements were recorded during the experiments, corresponding to different misalignments. Fig. 16 shows a snapshot of six out of twenty-one misalignment scenarios evaluated. The subfigure descriptions of Fig. 16 provide the horizontal and rotational misalignment position corresponding to each figure. The images corresponding to the rest are not provided in the interest of space. The variations in the parameters k, L_{Rx}, and L_{Tx} with the fabricated receiver coil's angular (*Angle*) and horizontal (*Delta X*) misalignments are shown in Fig. 17. Fig. 17(a)–(c) show the variations for coupler design 1. Fig. 17(d)–(f) show variations for design 3. The responses evaluated at selected misalignment positions are interpolated to depict the general pattern of parameter variation due to misalignments in each figure. The coupling coefficient reduction (Δk) due to misalignment is worse in the case of coupler design 1 compared to design 3, as seen in Table 10, Fig. 17(a) and (d). This result validates

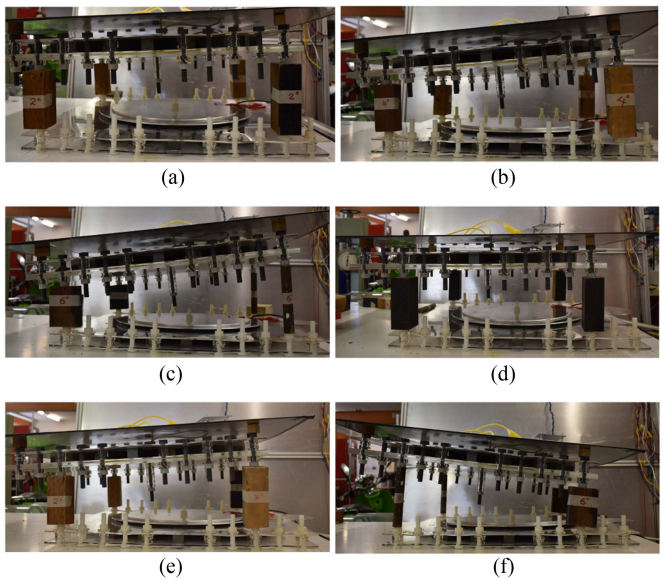

FIGURE 16. Snapshot of different misalignment scenarios evaluated using the hardware prototype. (a) (50 mm, 2^0). (b) (50 mm, 4^0). (c) (50 mm, 6^0). (d) (100 mm, 0^0). (e) (100 mm, 2^0). (f) (100 mm, -6^0).

that design 1 had a higher deviation than design 3 and justifies the selection of design 3 as the misalignment-tolerant design.

The impact of angular misalignment on L_{Rx} and L_{Tx} is minimal compared to the horizontal misalignment, and this is true for both designs, as seen in Fig. 17(b), (c), (e), and (f). The maximum variation of transmitter-side (L_{Tx}) and receiver-side (L_{Rx}) due to misalignment are 2.61 and 1.94 μH for design 3, while 3.34 and 2.04 μH for design 1 from their experimental nominal values given in Table 10. However, the L_{Rx} of design 3 lies within the range defined by (14). Therefore, its safety margins defined in Section III-E-3 and 4 are not violated, as confirmed during the design stage, as shown in Fig. 11 for L_{Rx}.

Fig. 18 shows the variation of L_{Tx} and L_{Rx} with air gaps. The air gap is the distance between the transmitter's top surface and the receiver's lowest contact point. This lowest contact point of the receiver varies with angular misalignment, as shown in Fig. 16. Therefore, the air gap variation happens due to angular misalignments. The angular misalignments are measured at 0^0, $\pm 2^0$, $\pm 4^0$, and $\pm 6^0$ intervals. The air gaps at these angular misalignment positions are approximately 150, 139, 129, and 119 mm for both designs, as shown in Fig. 18. Therefore, the maximum and minimum air gaps between the coils are 150 and 119 mm for designs 1 and 3. The maximum inductance variation in transmitter and receiver inductances given above is observed within this air gap range.

The maximum deviation of the transmitter side's resonant frequency due to inductance deviation is 0.63 kHz for design 1 and 0.48 kHz for design 3. The maximum variation of the receiver side's resonant frequency due to inductance deviation is 0.64 kHz for both designs 1 and 3. The resonant frequency variation is significantly smaller because of the smaller variation range in inductances due to misalignments.

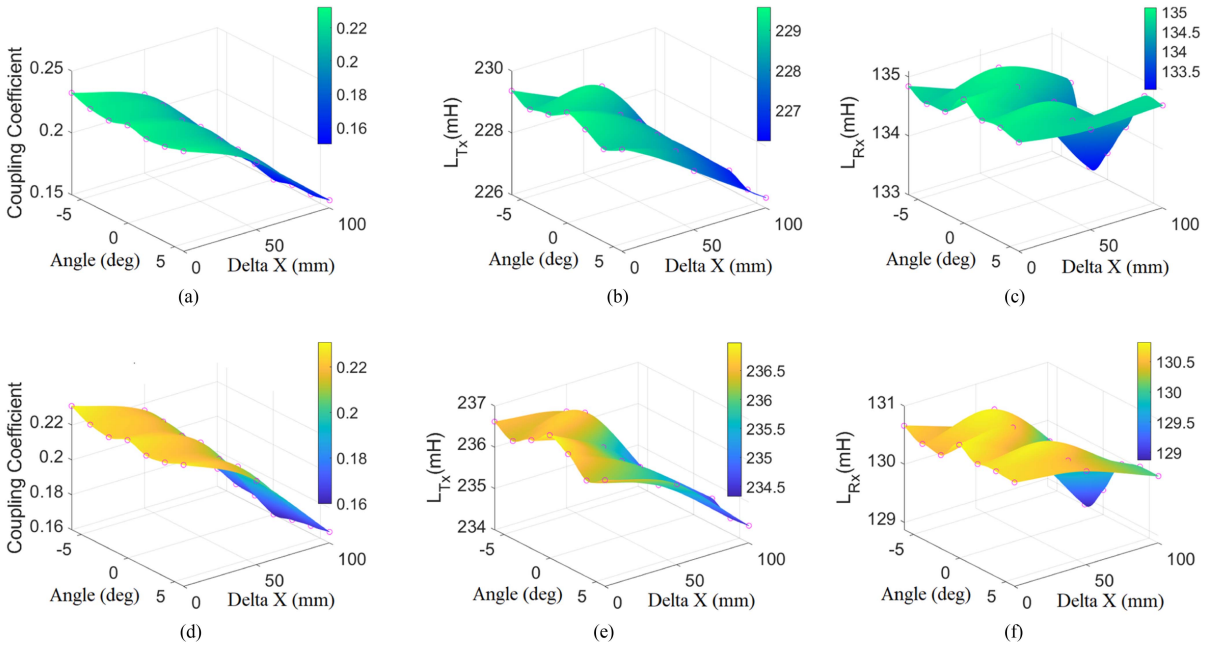

FIGURE 17. Misaligned experimental results. (a) Variation of k with angular and horizontal misalignment of design 1. (b) Variation of L_{Tx} with angular and horizontal misalignment of design 1. (c) Variation of L_{Rx} with angular and horizontal misalignment of design 1. (d). Variation of k with angular and horizontal misalignment of design 3. (e) Variation of L_{Tx} with angular and horizontal misalignment of design 3. (f) Variation of L_{Rx} with angular and horizontal misalignment of design 3.

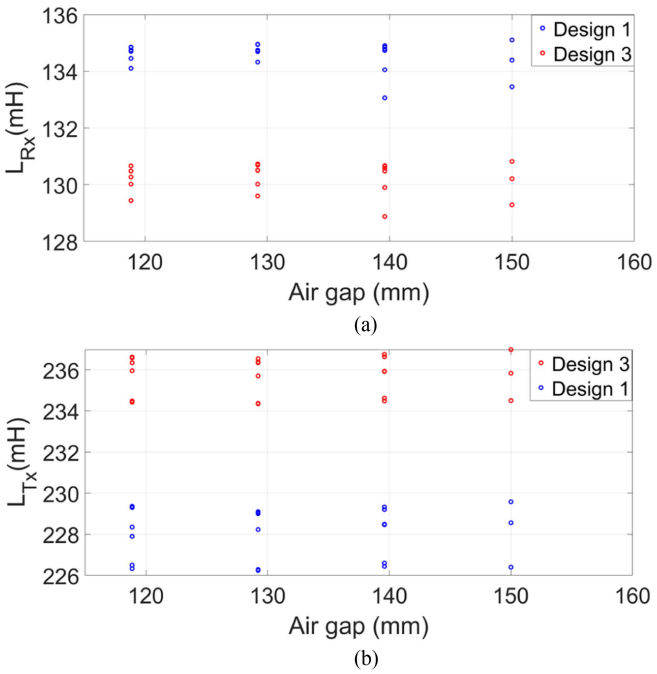

FIGURE 18. Variation of inductance with air gaps. (a) Receiver side inductance variation with air gaps. (b) Transmitter-side inductance variation with air gaps.

The change in self-inductances due to misalignments has minimal impact on the quality factors of the coil. According to (6), the efficiency will depend on the coils' coupling coefficient and quality factors. Both coupling and quality factors change simultaneously with misalignments. However, the coupling variation is significant (–34.5%) compared to the quality factor (–1.5%) for design 1. This observation is valid for design 3, as well. This behavior is also observed in Fig. 9 during the design stage. Therefore, coupling variation significantly impacts efficiency more than the quality factors or self-inductance variations when considering misalignments. The measured efficiency with misalignments of the receiver is shown in Fig. 19(a) and (b). The coupler design 3 has 94.52%, corresponding to a 100 mm horizontal offset and 0^0 angular offset. This is the coupler's lowest efficiency for any misalignment considered in this paper. However, coupler design 1 has 93.62% as the lowest efficiency, corresponding to the worst-case misalignment position of design 3. Therefore, the maximum efficiency deviation due to misalignments is 2.38% for design 3 and 3.33% for design 1. Design 3 has approximately 1% less deviation with misalignments. This confirms that design 3 has a better misalignment tolerance than design 1 and validates the efficacy of the proposed method. The reduction in efficiency in design 1 compared to design 3 is mainly related to the coupling coefficient in design 1 at the worst misalignment position is lower than that of design 3.

The leakage field is measured 650 mm from the center of the coupler using a Narda ELT 400 magnetic field meter. The leakage field plots corresponding to misalignments are shown in Fig. 19(c) and (d) for coil designs 3 and 1. The leakage magnetic field variation is minimal with angular misalignments, as seen in Fig. 19(c) and (d). However, horizontal misalignment has a higher impact on the leakage field. This was correctly

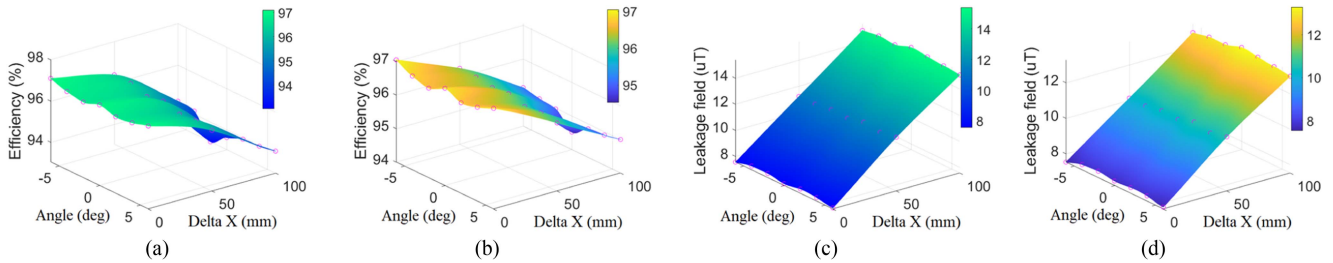

FIGURE 19. **Misaligned experimental results. (a) Variation of efficiency with misalignments of design 1. (b) Variation of efficiency with misalignments of design 3. (c) Variation of leakage field with misalignments of design 1. (d) Variation of leakage field with misalignments of design 3.**

identified during the design stage by misalignment sensitivity analysis, where Table 8 showed that horizontal misalignment had a high impact compared to angular misalignments. The coupler's leakage field increases to a maximum of 13.18 μT at (0^0, 100 mm) in design 3 and 15.28 μT at (0^0, 100 mm) in design 1. These results correspond to the highest leakage field reported for misalignments considered in this article. Both couplers' leakage field is well below the 27 μT limit defined in SAE J2954 STD and ICNIRP guideline, even with misalignments. However, design 3 has a lower leakage field compared to design 1.

D. DISCUSSION

The comparison between design 3 and design 1 shows that design 3 has higher efficiency and the lowest leakage magnetic field at the misaligned position. Moreover, the performances at the aligned position align with the Pareto-front results. Therefore, it validates that design 3 has a higher misalignment tolerance than design 1.

In literature, selecting a design for implementation from a conventional Pareto front of viable solutions lacks rational decision-making. More often, the objectives' values vary slightly, and it is hard to distinguish between the designs. In this optimization problem, the variation in efficiencies and leakage magnetic fields of designs 1 and 3 is 0.05% and 0.08 μT at the aligned position, as seen in Table 10 and Fig. 7. The decision to select a design for prototyping will be based on the designer's choice of this marginal difference, as both designs are Pareto-optimal. This article introduces misalignment tolerance as a decision-making factor in selecting a design from Pareto-front. It avoids user bias in choosing a Pareto-optimal design while incorporating misalignments in the design process. Design 3 had superior efficiency and the lowest leakage field at the worst misaligned position compared to design 1. Moreover, the efficiency difference is 0.9%, and the leakage field difference is 2.1 μT between design 1 and 3 at the worst-case misaligned positions. These differences are significant compared to differences at aligned positions and validate the significance of the proposed methodology.

This work demonstrated the efficacy of the proposed methodology with a circular coupler. However, it can be applied to other existing coupler structures because most coupler structures have similar design variables to circular couplers and experience similar misalignment scenarios discussed in Section II-B. The typical design variables of any coupler are the number of turns, the separation between the turns, the copper wire radius, dimensions of magnetic material and passive shield, the separation between winding and magnetic material, the separation between the magnetic material and passive shield, starting point of the windings, and starting point of the magnetic material if pieces are used. The proposed robust optimization method will optimize these design variables to derive the Pareto-front. Then, it will evaluate the misalignment tolerance of each design on the Pareto-front against the misalignment tolerance criteria defined in Section III-E-3 to determine the best misalignment-tolerant design. Therefore, the proposed method can be easily incorporated to realize a misalignment tolerant coupler configuration without compromising its performance at the aligned position.

As a future work, it would be interesting to perform a comparative study with different coupler configurations (DD, DDQ, Bipolar pad, and Tripolar pad) using this method to determine the improvement in misalignment tolerance of each coupler compared to conventional methods. Section I discusses different approaches to improving misalignment tolerance. Therefore, it would be interesting to develop a hybrid design methodology incorporating all these approaches to realize a superior misalignment-tolerant IPT system.

V. CONCLUSION

The coupler optimization is critical for improving the overall performance of an inductive power transfer system at aligned and misaligned positions. Therefore, this article introduced a method that aids in identifying the misalignment tolerant coupler design for hardware prototyping by considering misalignments as uncertainties to a perfectly aligned coupler. The proposed methodology also eliminates the designer bias in selecting a design for implementation from a Pareto-front. The misalignment criteria for determining the best design are defined based on the understanding gained through misalignment sensitivity analysis, where the SD of k, L_{Tx}, and L_{Rx} due to misalignments and the probability of violating the design limitations on L_{Rx} were considered. The experimental results demonstrated that the best misalignment-tolerant design outperforms other designs at worst-case misalignments while not

compromising its Pareto-optimal performance at the aligned position.

ACKNOWLEDGMENT

The authors acknowledge N. Harrisankar, M. Soltanian, R. Jacobs, and H. Salie for their assistance with setting up the experimental setup.

REFERENCES

[1] "Wireless charging of electric and plug-in hybrid vehicles, Society of Automotive Engineers," SAE Std. J2954, 2019. Accessed: Sep. 20, 2020. [Online]. Available: http://standards.sae.org/wip/j2954/

[2] IEC 61980-1:2015, "Electric vehicle wireless power transfer (WPT) systems - part 1: General requirements," 2015. Accessed: Sep. 20, 2020. [Online]. Available: https://webstore.iec.ch/publication/22951

[3] "ISO 19363:2020: Electrically propelled road vehicles — Magnetic field wireless power transfer — Safety and interoperability requirements," 2020. Accessed: Sep. 20, 2020. [Online]. Available: https://www.iso.org/obp/ui/#iso:std:iso:19363:ed-1:v1:en

[4] S. Jayalath and A. Khan, "Analysis of the relationship between the parameters of IPT transformer and power electronic system," in *Proc. IEEE Wireless Power Transf. Conf.*, 2017, pp. 1–4.

[5] S. Jayalath and A. Khan, "Design, challenges, and trends of inductive power transfer couplers for electric vehicles: A review," *IEEE J. Emerg. Sel. Topics Power Electron.*, vol. 9, no. 5, pp. 6196–6218, Oct. 2021.

[6] R. Bosshard, J. W. Kolar, J. Mühlethaler, F. Canales, I. Stevanovi´c, and B. Wunsch, "Modeling and η - α-pareto optimization of inductive power transfer coils for electric vehicles," *IEEE J. Emerg. Sel. Topics Power Electron.*, vol. 3, no. 1, pp. 50–64, Mar. 2015.

[7] H. Kim et al., "Coil design and measurements of automotive magnetic resonant wireless charging system for high-efficiency and low magnetic field leakage," *IEEE Trans. Microw. Theory Techn.*, vol. 64, no. 2, pp. 383–400, Feb. 2016.

[8] M. Moghaddami, A. Anzalchi, A. Moghadasi, and A. Sarwat, "Pareto optimization of circular power pads for contactless electric vehicle battery charger," in *Proc. IEEE Ind. Appl. Soc. Annu. Meet.*, 2016, pp. 1–6.

[9] R. Bosshard, U. Iruretagoyena, and J. W. Kolar, "Comprehensive evaluation of rectangular and double-D coil geometry for 50 kW/85 kHz IPT system," *IEEE J. Emerg. Sel. Topics Power Electron.*, vol. 4, no. 4, pp. 1406–1415, Dec. 2016.

[10] S. Bandyopadhyay, V. Prasanth, P. Bauer, and J. A. Ferreira, "Multi-objective optimisation of a 1-kW wireless IPT systems for charging of electric vehicles," in *Proc. IEEE Transp. Electrific. Conf. Expo*, 2016, pp. 1–7.

[11] T. Yilmaz, N. Hasan, R. Zane, and Z. Pantic, "Multi-objective optimization of circular magnetic couplers for wireless power transfer applications," *IEEE Trans. Magn.*, vol. 53, no. 8, Aug. 2017, Art. no. 8700312.

[12] M. Lu and K. D. T. Ngo, "A fast method to optimize efficiency and stray magnetic field for inductive-power-transfer coils using lumped-loops model," *IEEE Trans. Power Electron.*, vol. 33, no. 4, pp. 3065–3075, Apr. 2018.

[13] A. A. S. Mohamed, S. An, and O. Mohammed, "Coil design optimization of power pad in IPT system for electric vehicle applications," *IEEE Trans. Magn.*, vol. 54, no. 4, Apr. 2018, Art. no. 9300405.

[14] Z. Li, H. Liu, Y. Huo, J. He, Y. Tian, and J. Liu, "High-misalignment tolerance wireless charging system for constant power output using dual transmission channels with magnetic flux controlled inductors," *IEEE Trans. Power Electron.*, vol. 37, no. 11, pp. 13930–13945, Nov. 2022.

[15] X. Qing, Y. Su, A. P. Hu, X. Dai, and Z. Liu, "Dual-loop control method for CPT system under coupling misalignments and load variations," *IEEE J. Emerg. Sel. Topics Power Electron.*, vol. 10, no. 4, pp. 4902–4912, Aug. 2022.

[16] A. Berger, M. Agostinelli, S. Vesti, J. A. Oliver, J. A. Cobos, and M. Huemer, "A wireless charging system applying phase-shift and amplitude control to maximize efficiency and extractable power," *IEEE Trans. Power Electron.*, vol. 30, no. 11, pp. 6338–6348, Nov. 2015.

[17] A. Ramezani and M. Narimani, "Optimized electric vehicle wireless chargers with reduced output voltage sensitivity to misalignment," *IEEE J. Emerg. Sel. Topics Power Electron.*, vol. 8, no. 4, pp. 3569–3581, Dec. 2020.

[18] H. Zhu, B. Zhang, and L. Wu, "Output power stabilization for wireless power transfer system employing primary-side-only control," *IEEE Access*, vol. 8, pp. 63735–63747, 2020.

[19] Z. Huang, S.-C. Wong, and C. K. Tse, "Control design for optimizing efficiency in inductive power transfer systems," *IEEE Trans. Power Electron.*, vol. 33, no. 5, pp. 4523–4534, May 2018.

[20] Y. Jiang, L. Wang, J. Fang, C. Zhao, K. Wang, and Y. Wang, "A joint control with variable ZVS angles for dynamic efficiency optimization in wireless power transfer system," *IEEE Trans. Power Electron.*, vol. 35, no. 10, pp. 11064–11081, Oct. 2020.

[21] Y. Chen, B. Yang, Z. Kou, Z. He, G. Cao, and R. Mai, "Hybrid and reconfigurable IPT systems with high-misalignment tolerance for constant current and constant voltage battery charging," *IEEE Trans. Power Electron.*, vol. 33, no. 10, pp. 8259–8269, Oct. 2018.

[22] L. Zhao, D. J. Thrimawithana, U. K. Madawala, A. P. Hu, and C. C. Mi, "A misalignment-tolerant series-hybrid wireless EV charging system with integrated magnetics," *IEEE Trans. Power Electron.*, vol. 34, no. 2, pp. 1276–1285, Feb. 2019.

[23] Z. Liu, M. Su, Q. Zhu, L. Zhao, and A. P. Hu, "A dual-frequency tuning method for improved coupling tolerance of wireless power transfer system," *IEEE Trans. Power Electron.*, vol. 36, no. 7, pp. 7360–7365, Jul. 2021.

[24] J. Mai, Y. Wang, Y. Yao, and D. Xu, "Analysis and design of high misalignment tolerant compensation topologies with constant current or constant-voltage output for IPT systems," *IEEE Trans. Power Electron.*, vol. 36, no. 3, pp. 2685–2695, Mar. 2021.

[25] W. Li, H. Zhao, J. Deng, S. Li, and C. C. Mi, "Comparison study on SS and double-sided LCC compensation topologies for EV/PHEV wireless chargers," *IEEE Trans. Veh. Technol.*, vol. 65, no. 6, pp. 4429–4439, Jun. 2016.

[26] J. Yang, X. Zhang, K. Zhang, X. Cui, C. Jiao, and X. Yang, "Design of LCC-S compensation topology and optimization of misalignment tolerance for inductive power transfer," *IEEE Access*, vol. 8, pp. 191309–191318, 2020.

[27] Y. Yao, Y. Wang, X. Liu, K. Lu, and D. Xu, "Analysis and design of an S/SP compensated IPT system to minimize output voltage fluctuation versus coupling coefficient and load variation," *IEEE Trans. Veh. Technol.*, vol. 67, no. 10, pp. 9262–9272, Oct. 2018.

[28] G. Ke, Q. Chen, L. Xu, X. Ren, and Z. Zhang, "Analysis and optimization of a double-sided S-LCC hybrid converter for high misalignment tolerance," *IEEE Trans. Ind. Electron.*, vol. 68, no. 6, pp. 4870–4881, Jun. 2021.

[29] F. Wang, J. Zhu, A. Sun, and B. Liu, "Multi-objective optimization of double-D orthogonal coil in the underwater environment," in *Proc. IEEE 6th Inter. Electric. Energy Conf.*, 2023, pp. 2296–2301.

[30] A. Hariri, A. Elsayed, and O. A. Mohammed, "An integrated characterization model and multiobjective optimization for the design of an EV charger's circular wireless power transfer pads," *IEEE Trans. Magn.*, vol. 53, no. 6, Jun. 2017, Art. no. 8001004.

[31] M. A. Moya, A. Delgado, and M. Vasic, "Multi-objective optimization for DC transformer based on inductive power transfer technology for future electric transport," in *Proc. Wireless Power Week*, 2022, pp. 509–513.

[32] D. Kraus and H. Herzog, "Magnetic design of a Q-coil for a 10 kW DDQ system for inductive power transfer," in *Proc. IEEE PELS Workshop Emerg. Technol. Wireless Power*, 2019, pp. 140–143.

[33] G. A. Covic, M. L. G. Kissin, D. Kacprzak, N. Clausen, and H. Hao, "A bipolar primary pad topology for EV stationary charging and highway power by inductive coupling," in *Proc. IEEE Energy Convers. Congr. Expo.*, 2011, pp. 1832–1838.

[34] M. Abdelraziq, S. Paul, F. Bartels, and Z. Pantic, "Optimization of efficiency and receiver-coil mass in an autonomous 700-W S-S IPT system for UAV applications," in *Proc. IEEE Appl. Power Electron. Conf. Expo.*, 2023, pp. 803–810.

[35] M. Mohammad, S. Choi, Z. Islam, S. Kwak, and J. Baek, "Core design and optimization for better misalignment tolerance and higher range of wireless charging of PHEV," *IEEE Trans. Transp. Electrific.*, vol. 3, no. 2, pp. 445–453, Jun. 2017.

[36] J. P. K. Sampath, A. Alphones, and D. M. Vilathgamuwa, "Figure of merit for the optimization of wireless power transfer system against misalignment tolerance," *IEEE Trans. Power Electron.*, vol. 32, no. 6, pp. 4359–4369, Jun. 2017.

[37] S. Bandyopadhyay, P. Venugopal, J. Dong, and P. Bauer, "Comparison of magnetic couplers for IPT-based EV charging using multi-objective optimization," *IEEE Trans. Veh. Technol.*, vol. 68, no. 6, pp. 5416–5429, Jun. 2019.
[38] Z. Luo, X. Wei, M. G. S. Pearce, and G. A. Covic, "Multiobjective optimization of inductive power transfer double-D pads for electric vehicles," *IEEE Trans. Power Electron.*, vol. 36, no. 5, pp. 5135–5146, May 2021.
[39] W. Shi et al., "Design of a highly efficient 20-kW inductive power transfer system with improved misalignment performance," *IEEE Trans. Transp. Electrific.*, vol. 8, no. 2, pp. 2384–2399, Jun. 2022.
[40] Y. Otomo and H. Igarashi, "A 3-D topology optimization of magnetic cores for wireless power transfer device," *IEEE Trans. Magn.*, vol. 55, no. 6, Jun. 2019, Art. no. 8103005.
[41] R. Bosshard, J. W. Kolar, and B. Wunsch, "Control method for inductive power transfer with high partial-load efficiency and resonance tracking," in *Proc. Int. Power Electron. Conf.*, May 2014, pp. 2167–2174.
[42] T. Most and J. Will, "Sensitivity analysis using the metamodel of optimal prognosis," in *Proc. Weimarer Optimierungs- und Stochastiktage 8.0*, Nov. 2011.
[43] T. Most and J. Will, "Metamodel of Optimal Prognosis - an automatic approach for variable reduction and optimal metamodel selection," in *Proc. Weimarer Optimierungs-und Stochastiktage*, 2008, pp. 20–21.
[44] D. Roos, U. Adam, and C. Bucher, "Robust design optimization," in *Proc. Weimar Optim. Stochastic Days 3.0*, 2006, pp. 1–22.
[45] D. Roos, J. Einzinger, and V. Bayer, "Robust design optimization applied to structural, thermal and fluid analysis including manufacturing tolerances," in *Proc. Weimarer Optimierungs- und Stochastiktage 6.0*, 2009, pp. 1–22.
[46] D. Roos, K. Cremanns, and T. Jasper, "Probability and variance-based stochasic design optimization of a radial compressor concerning fluid-structure interaction," in *Proc. Int. Conf. Comput. Meth. Coup. Prob. Sci. Eng.*, 2013, pp. 1–27.
[47] "optiSLang - Software for CAE-based Robust Design Optimization and FE-analysis," DYNARDO, Weimar, 2019. Accessed: Sep. 20, 2020. [Online]. Available: www.dynardo.de

SAMPATH JAYALATH (Member, IEEE) received the B.Eng. (Hons.) degree in electronic engineering from Sheffield Hallam University, Sheffield, U.K, in 2013, and the M.Sc. and Ph.D. degrees in electrical engineering from the University of Cape Town (UCT), Cape Town, South Africa, in 2016 and 2022, respectively.

He is currently with the Department of Electrical Engineering, UCT, where he is currently a Lecturer. He is also the Chair of the IEEE IAS/IES/PELS combined South Africa chapter. His research interests include filter design, digital control of power converters, wireless power transfer, biomedical devices, and electromagnetic robotics.

AZEEM KHAN (Senior Member, IEEE) received the B.Sc. Eng., M.Sc., and Ph.D. degrees in electrical engineering from the University of Cape Town, Cape Town, South Africa, in 1994, 2001, and 2006, respectively.

He worked previously with the Electricity Utility in South Africa, Eskom, as a Maintenance Engineer and System Engineer on the turbine and generator control systems. He is currently with the Department of Electrical Engineering, University of Cape Town in South Africa, where he is currently a Professor. His research interests include permanent magnet machine design and control of renewable energy systems.